3   Electronic Spectroscopy of the Au-Ar complex

3.1   Introduction

The $X^2\Sigma_{1/2}^+$, $D^2\Pi_{1/2}$ and $D^2\Pi_{3/2}$ states of Au-Ar have been investigated previously by Knight *et al.*,[1] employing a (1+1) REMPI scheme, as one of a number of studies on coinage metal – rare gas complexes; the bulk of which has been summarized in Chapter 1.   In the previous work a number of spectroscopic constants were derived for the $D^2\Pi_{1/2}$ and $D^2\Pi_{3/2}$ excited states through the fitting of the observed vibrational levels to the usual Morse expression.   A value for the excited state dissociation limit, D_L, was determined by a LeRoy-Bernstein extrapolation, which subsequently allowed the ground state dissociation energy, D_0'', to be derived.   A summary of these spectroscopic constants, by Knight *et al.* are given in Table 3.1.

In the investigation by Knight *et al.* a number of observations were made with regard to their presented spectra.   The first was that the red shifting of the spectra with regard to the corresponding atomic transitions indicates that these observed excited states are more strongly bound than the ground state; which, as discussed in Chapter 1 is a result of a difference in the spatial orientation of the electron density in these excited states compared to the ground state.   The significantly different appearance of the spectra of the two observed $^2\Pi$ spin-orbit split states was considered to be a result of spin–orbit interactions between states of the same Ω value; the $D^2\Pi_{1/2}$ state and

the $E^2\Sigma_{1/2}^+$ state. This spin-orbit interaction was hypothesized to lead to extensive mixing between these molecular states, resulting in the $D^2\Pi_{1/2}$ state being less bound than expected owing to a contribution of Σ character from the spin-orbit interaction with the $E^2\Sigma_{1/2}^+$ state. Conversely the unobserved $E^2\Sigma_{1/2}^+$ state was hypothesized to be less repulsive than expected owing to a contribution of Π character. As the $D^2\Pi_{3/2}$ state was envisaged to remain unaffected by this spin orbit interaction to first order, the observed difference in binding energy between the two states could be rationalized.

Table 3.1. Summary of spectroscopic constants derived in reference 1.

	$D^2\Pi_{1/2}$	$D^2\Pi_{3/2}$
ω_e' (cm^{-1})	73.3[a]	79.4[a]
$\omega_e'x_e'$ (cm^{-1})	3.77[a]	1.93[a]
D_0' (cm^{-1})	≥338[b]	≥654[b]
D_0'' (cm^{-1})	128[c]	206[c]

[a] Determined by fitting observed points to Morse potential of form $E(v) = a\,(v + 1/2) - \omega_e'x_e'\,(v + 1/2)^2$ where a is a lower limit for ω_e'.

[b] Determined from energy span of observed features.

[c] Determined by subtraction of Au ($^2P_J \leftarrow {}^2S_{1/2}$) excitation energy from D_L estimated *via* a LeRoy-Bernstein extrapolation.

Reinvestigating the work of Knight *et al.* in the present study provides additional information and insight into the $X^2\Sigma_{1/2}^+$, $D^2\Pi_{1/2}$ and $D^2\Pi_{3/2}$ states in Au-Ar obtained through both experimental and theoretical procedures. Owing to the presence of only one abundant naturally occurring isotope of ^{197}Au (100%) and ^{40}Ar (99.603%)[2] Knight *et al.* were unable to determine the absolute vibrational numbering through the usual analysis of isotopic shifts. However in this study the absolute vibrational numbering of the $D^2\Pi_{3/2}$ state has been estimated by comparison of theoretical and experimental results.

3.2 Experimental

The experimental procedure has been described in detail in Chapter 2 so only a brief description of the experiment is outlined here. Au-Ar complexes were generated by pulsing pure Ar, held at a pressure of 7-10 bar, over a Au rod held within the LaVa source. Au atoms ablated by the second harmonic of a Nd:YAG laser (Continuum Minilite II) were seeded into the gas pulse which flowed through the cooling channel, before expanding into the high vacuum region of the chamber. The Au-Ar clusters formed in the resulting expansion travelled to the extraction region of the ionization chamber where they were ionized and detected. A +110 V difference across the repeller plates that was used to direct the ions up the TOF tube to the MCPs with the lower plate set at +770 V and the upper plate set at +660 V.

The frequency doubled output of a Sirah dye laser was focused into the extraction region of the ionization chamber leading to ionization of the Au-Ar complexes in a (1+1) REMPI scheme. The dye laser used Coumarin 540A and 480 dyes for the $D^2\Pi_{1/2}$ and $D^2\Pi_{3/2}$ states respectively and was pumped by the third harmonic of a Surelite III Nd: YAG laser.

3.3 Results

3.3.1 $D^2\Pi_{1/2} \leftarrow X^2\Sigma_{1/2}^+$ and $D^2\Pi_{3/2} \leftarrow X^2\Sigma_{1/2}^+$ spectra

The spectrum recorded in the vicinity of the $^2P_{1/2} \leftarrow {}^2S_{1/2}$ atomic Au transition is shown in Figure 3.1 with the line positions reported in

Table 3.2. The spectrum is similar in appearance to that previously reported by Knight *et al.*, with an additional feature here observed to higher energy. From initial inspection of the spectrum, it can be seen that the spacing between adjacent features dramatically decreases as the progression continues to higher energy. The rotational profile of these higher energy features also differs from those at the start of the progression; they are observed to be narrow and red degraded (asymmetrical with the tail going to lower energy) while the features to lower energy are broader and are blue degraded (asymmetrical with the tail going to higher energy). Since the spectrum extends to the red of the atomic Au ($^2P_{1/2}$) transition, $T_{1/2}$, a D_0'' value of ≥ 124 cm^{-1} can be estimated. (Improvements to this experimental value are obtained by using extrapolation procedures that are discussed in section 3.3.2). An excited state dissociation energy, D_0', of ≥ 347.8 cm^{-1} can then be derived for the $D^2\Pi_{1/2}$ state.

Table 3.2. Line positions for $D^2\Pi_{1/2} \leftarrow X^2\Sigma_{1/2}^+$ spectrum shown in Figure 3.1. The first observed peak is denoted as *n*.

Wavenumber (cm^{-1})	Assignment	Wavenumber (cm^{-1})	Assignment
37135.7	$n \leftarrow 0$	37382.7	$n + 7 \leftarrow 2$
37154.4	$n + 1 \leftarrow 2$	37389.6	$n + 5 \leftarrow 0$
37177.8	$n + 1 \leftarrow 1$	37391.6	$n + 6 \leftarrow 1$
37200.1	$n + 1 \leftarrow 0$	37398.5	$n + 8 \leftarrow 2$
37233.2	$n + 2 \leftarrow 1$	37407.4	$n + 7 \leftarrow 1$
37258.4	$n + 2 \leftarrow 0$	37416.3	$n + 6 \leftarrow 0$
37272.5	$n + 3 \leftarrow 2$	37425.3	$n + 8 \leftarrow 1$
37286.1	$n + 3 \leftarrow 1$	37436.2	$n + 7 \leftarrow 0$
37309.8	$n + 3 \leftarrow 0$	37450.4	$n + 8 \leftarrow 0$
37320.6	Unassigned	37458.1	$n + 11 \leftarrow 1$
37331.5	$n + 4 \leftarrow 1$	37462.6	$n + 9 \leftarrow 0$
37354.3	$n + 4 \leftarrow 0$	37473.2	$n + 10 \leftarrow 0$
37363.8	$n + 5 \leftarrow 1$	37483.5	$n + 11 \leftarrow 0$
37366.3	$n + 6 \leftarrow 2$		
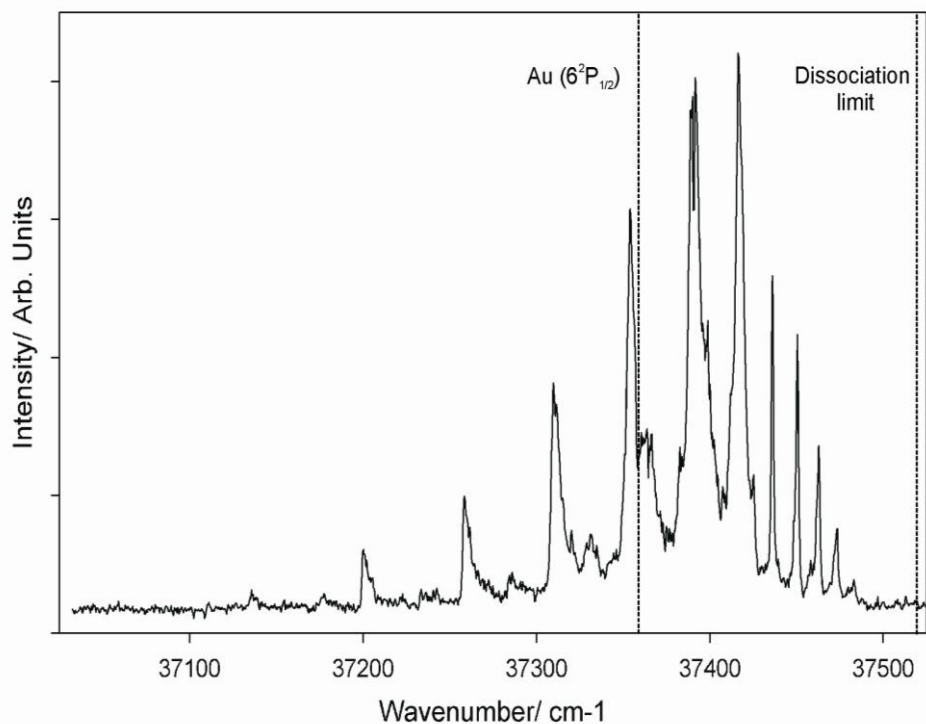
Figure 3.1. Spectrum of Au-Ar corresponding to the $D^2\Pi_{1/2} \leftarrow X^2\Sigma_{1/2}^+$ transition. The dissociation limit is obtained from $T_{1/2} + D_0''$, where the ground state dissociation energy was determined from *ab initio* calculations (discussed in section 3.4.1).

The spectrum recorded in the vicinity of the $^2P_{3/2} \leftarrow {}^2S_{1/2}$ atomic Au transition is shown in Figure 3.2, with the corresponding line positions reported in Table 3.3. This spectrum has an improved overall signal-to-noise ratio compared to the spectrum reported by Knight *et al.* This is most apparent to higher energies where the signal-to-noise was particularly poor in that work, owing to problems obtaining UV in this region. In stark contrast to the $D^2\Pi_{1/2}$ state, the spacings and rotational peak profiles for the $D^2\Pi_{3/2}$ state appear consistent throughout the spectrum. As with the $D^2\Pi_{1/2}$ state it is unlikely, given the Franck – Condon profile, that the electronic origin is observed. The energy span of the spectrum allows a lower limit for

D_0' of 731.7 cm^{-1} to be estimated; a value considerably greater than that of the $D^2\Pi_{1/2}$ state.

Table 3.3. Line positions for $D^2\Pi_{3/2} \leftarrow X^2\Sigma_{1/2}^+$ spectrum shown in Figure 3.2. The first observed peak is denoted as n.

Wavenumber (cm^{-1})	Assignment	Wavenumber (cm^{-1})	Assignment
40401.6	$n \leftarrow 0$	40760.7	$n + 5 \leftarrow 0$
40456.8	$n + 1 \leftarrow 1$	40797.8	$n + 6 \leftarrow 1$
40480.9	$n + 1 \leftarrow 0$	40819.9	$n + 6 \leftarrow 0$
40510.0	$n + 2 \leftarrow 2$	40876.0	$n + 7 \leftarrow 0$
40533.1	$n + 2 \leftarrow 1$	40928.1	$n + 8 \leftarrow 0$
40557.2	$n + 2 \leftarrow 0$	40952.1	$n + 9 \leftarrow 1$
40583.2	$n + 3 \leftarrow 2$	40978.2	$n + 9 \leftarrow 0$
40606.3	$n + 3 \leftarrow 1$	41021.2	$n + 10 \leftarrow 0$
40628.4	$n + 3 \leftarrow 0$	41061.3	$n + 11 \leftarrow 0$
40652.4	$n + 4 \leftarrow 2$	41099.3	$n + 12 \leftarrow 0$
40673.5	$n + 4 \leftarrow 1$	41109.3	$n + 13 \leftarrow 1$
40696.6	$n + 4 \leftarrow 0$	41133.3	$n + 13 \leftarrow 0$
40737.7	$n + 5 \leftarrow 1$		
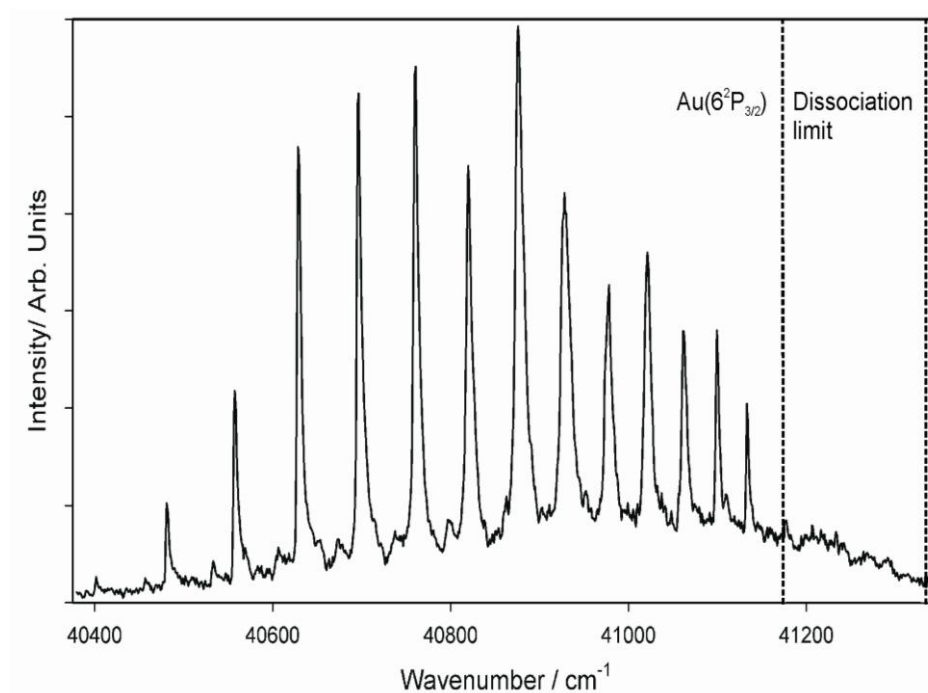
Figure 3.2. Spectrum of Au-Ar corresponding to the $D^2\Pi_{3/2} \leftarrow X^2\Sigma_{1/2}^+$ transition. The dissociation limit is obtained from $T_{3/2} + D_0''$, where the ground state dissociation energy was determined from *ab initio* calculations (discussed in section 3.4.1).

-51-

3.3.2 Extrapolation procedures for determining spectroscopic constants

When a number of vibrational levels are observed, it is possible to determine a number of spectroscopic constants for the observed state from an analysis of the spacings between them. The dissociation energy of a particular energy state can be simply thought of as the sum of the energy spacings between vibrational levels, $\Delta G_{v+1/2}$, starting from $v = 0$.

$$D_0 = \sum_v \Delta G_{v+1/2} \qquad (3.1)$$

Assuming all the vibrational levels are known, the dissociation energy can be determined. However, in most cases the actual observed features represent only a portion of the total number of vibrational levels in that particular state. This problem can be overcome by assuming that that the potential energy curve can be described by the Morse expression and so the energies of the vibrational energy levels are given by:

$$G(v) = \omega_e (v + \tfrac{1}{2}) - \omega_e x_e (v + \tfrac{1}{2})^2 \qquad (3.2)$$

In which ω_e is the harmonic vibrational frequency and x_e is the anharmonicity constant. The spacings between adjacent levels are then given by:[3]

$$\Delta G_{v+1/2} = \omega_e - 2\omega_e x_e (v + 1) \qquad (3.3)$$

in which v is the lower vibrational level. If the absolute vibrational numbering is known, then a plot of $\Delta G_{v+\frac{1}{2}}$ versus $v + 1$ can be extrapolated to $\Delta G_{v+\frac{1}{2}} = 0$, allowing D_0 to be estimated[3] by integrating the area under the plot, often referred to as a Birge-Sponer plot. As can be seen from equations 3.3 and 3.2 the spectroscopic constants ω_e and $\omega_e x_e$ are easily obtained from the intercept and gradient of the plot respectively or alternatively by direct fitting of the line positions to the Morse expression. From ω_e and $\omega_e x_e$ it is trivial to derive D_e from the following equation:[4]

$$D_e = \frac{\omega_e^{\,2}}{4\omega_e x_e} \tag{3.4}$$

As can be seen from the above, the use of the Morse approximation is a convenient way to describe the potential energy curve of a system; however, it should not be forgotten that it is only an approximation. This is particularly relevant for vibrational levels observed which are high in the potential well where the anharmonicity of the potential is less well described by the Morse expression, leading to analyses such as Birge-Sponer plots overestimating dissociation energies. In these situations a LeRoy-Bernstein extrapolation is considered to be more appropriate as it is designed to account for the curvature (resulting in the over estimation of D_0) often observed in Birge-Sponer plots near the dissociation limit, D_L, where long range intermolecular forces become more important.

In the most common situation the long-range part of a potential, $V(R)$, can be closely approximated by

$$V(R) = D_L - (C_n / R^n) \qquad (3.5)$$

in which R is the internuclear separation and C is a constant depending on the identity of the atoms[5] The distribution of vibrational energy levels $E(v)$ near D_L is closely approximated by

$$\frac{d}{dv}[E(v)] = K_n[D_L - E(v)]^{[(n+2)/2n]} \qquad (3.6)$$

where, K_n is a constant.[6] If the vibrational levels in the potential are sufficiently dense, the approximation below can be used,[7]

$$\frac{dE(v)}{dv} \approx \overline{\Delta G_v} \equiv \frac{1}{2}[\Delta G_{v-1/2} + \Delta G_{v+1/2}] = \frac{1}{2}[E(v-1) + E(v+1)] \quad (3.7)$$

Substitution of equation 3.7 into equation 3.6 yields the following expression[7]

$$\overline{(\Delta G_v)}^{[2n/n+2]} = [D_L - E(v)](K_n)^{[(n+2)/2n]} \qquad (3.8)$$

Using equation 3.8, a simple plot of $\Delta G_v{}^{(2n/n+2)}$ against $E(v)$ will allow D_L to be evaluated. If the state of interest is an excited state its dissociation energy, D_0', can then be determined if the electronic origin, T_0, is known.
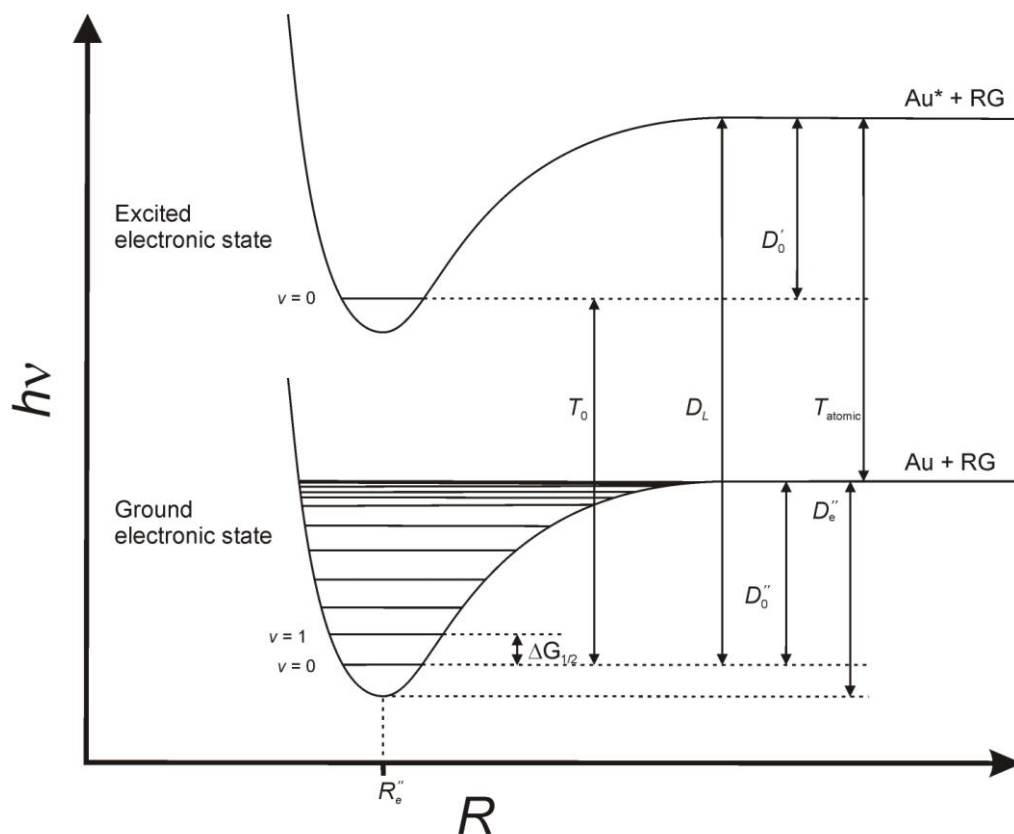
Figure 3.3. A summary of the spectroscopic constants used, or determined, in Section 3.3.2 and in the analysis of Au-RG spectra. From equation 3.3 it can be seen that $\Delta G_{½}$ will be equal to $\omega_e - 2\omega_e x_e$.

Both the Birge-Sponer and LeRoy-Bernstein methods are useful for the determination of dissociation energies when only a number of vibrational levels are observed. In the experiments carried out within the present work the vibrational levels observed are those of an excited state. However, the dissociation of the ground state can also be obtained by use of the following expression[3]

$$D_0'' = D_0' + T_0 - T_{atomic} \tag{3.9}$$

in which T_{atomic} is the energy of the specific atomic transition used. $D_0' + T_0$ gives the energy at the dissociation limit of the excited state, hence D_0'' can be calculated directly from a LeRoy-Bernstein plot if the atomic transition is known. Figure 3.3 gives a summary of the spectroscopic quantities described for both the ground and excited electronic states and the energies that relate to the transitions between them.

In Figure 3.4(a) a LeRoy-Bernstein plot is shown for the $D^2\Pi_{1/2}$ state, using the peak positions reported in Table 3.2. For Au-Ar it is expected that the long-range intermolecular forces will be dominated by an induced dipole – induced dipole interaction, which have a $1/R^6$ dependence. Using this dependence of $1/R^6$ in equation 3.8, $\Delta G_{v'}$ is plotted to the power of $^3/_2$. It is interesting to note that the last three points in the $D^2\Pi_{1/2}$ plot can be seen to deviate from the trend expected by the curvature of the other points in the analysis; these are the markedly different peaks observed in the progression. Taking this into consideration, separate analyses were performed for the first set of peaks ($n – n+6$) and the last set of peaks ($n+7 – n+11$); the results of these analyses are shown in Table 3.4.

Table 3.4. Results of LeRoy-Bernstein and vibrational spacing analysis for the $D^2\Pi_{1/2}$ state. Details in text.

	LeRoy-Bernstein			Vibrational spacings analysis		
	Overall	(n - n+6)	(n+7 – n+11)	Overall	(n - n+6)	(n+7 – n+11)
D_L (cm^{-1})	37485.8	37506.5	37528.8	37541.3	37564.1	37556.2
D_0'' (cm^{-1})	126.8	147.6	169.8	182.3	205.1	197.2
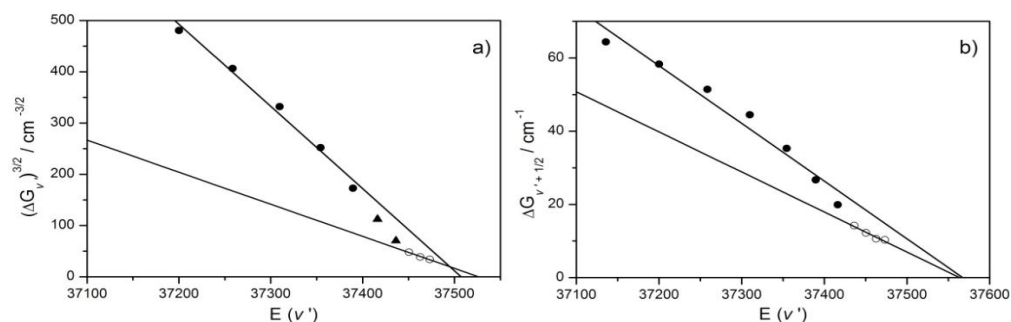
Figure 3.4. **LeRoy-Bernstein plot (a) and plot of vibrational spacings against wavenumber (b) for vibrational features observed for the $D^2\Pi_{1/2}$ state. The solid circles represent the analysis of the first set of features (n - $n+6$), whilst open circles represent the analysis of the last set of features ($n+7$ – $n+11$).**

Figure 3.5(a) shows a LeRoy-Bernstein plot for the $D^2\Pi_{3/2}$ state, using the peak positions reported in Table 3.3. Figure 3.5(b) shows the Birge-Sponer analysis for the $D^2\Pi_{3/2}$ state, using the absolute vibrational numbering shown in Figure 3.8, determined through computational methods (see later). The results of the LeRoy-Bernstein and Birge-Sponer analyses of the vibrational levels of the $D^2\Pi_{3/2}$ state are shown in Table 3.5. As it was not possible to determine the vibrational numbering for the $D^2\Pi_{1/2}$ state an equivalent plot of vibrational spacings against energy was performed, again the discontinuity in the higher energy points is observed; hence further plots were performed for the separate sets of data. The two plots are shown in Figure 3.4b with the derived spectroscopic constants from this plot shown in Table 3.4.

Table 3.5. Results of LeRoy-Bernstein and Birge-sponer analysis for $D^2\Pi_{3/2}$ state.

	D_0' (cm^{-1})	ω'_e (cm^{-1})	$\omega'_e x'_e$ (cm^{-1})	D_L (cm^{-1})	D_0'' (cm^{-1})
$D^2\Pi_{3/2}$ (LB)				41385.78	211.16
$D^2\Pi_{3/2}$ (BS)	1804.19	117.68	1.92		85.80[a]

[a] Calculated using T_0 derived by fitting spacings to a Morse potential
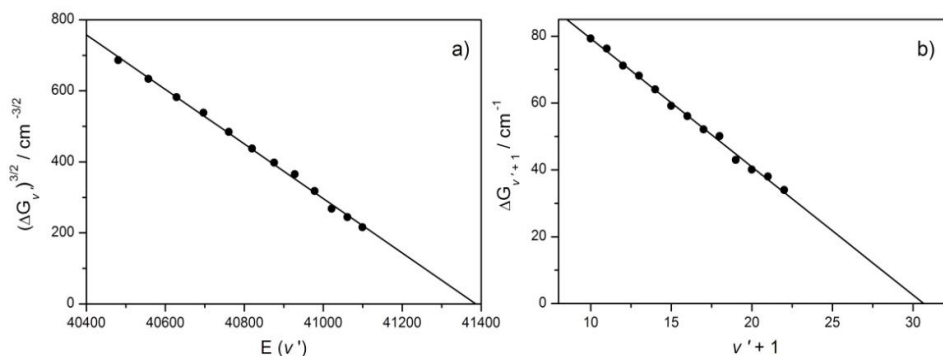
Figure 3.5. LeRoy-Bernstein (a) and Birge-Sponer (b) analysis of vibrational features observed in $D^2\Pi_{3/2}$ spectrum. In which v is that determined in Section 3.4.3.

3.4 Calculations

To complement experimental results, a number of calculations were performed by members of the research group; a description of these calculations is given within this work. The aim of these calculations was to determine potential energy curves for the $X^2\Sigma_{1/2}^+$, $D^2\Pi_{1/2}$, $D^2\Pi_{3/2}$, and $E^2\Sigma_{1/2}^+$ states, from which spectroscopic constants could be derived.

All calculations described herein were performed in MOLPRO.[8] For the Ar all-electron d-aug-cc-pVXZ basis sets were employed (X = Q, 5), while for Au the relativistic core potential ECP60MDF was used, augmented with the corresponding d-aug-cc-pVXZ-PP basis set.[9] For simplicity, these will be referred to by d-aVQZ and d-aV5Z.

3.4.1 Calculations on the $X^2\Sigma^+_{1/2}$ ground state

The first and simplest calculations performed investigated the Au-Ar $X^2\Sigma_{1/2}^+$ ground state at the RCCSD(T) level of theory, employing the

-58-

d-aVQZ and *d*-aV5Z basis sets. It is expected that the RCCSD(T) method will recover a significant proportion of the dynamic correlation energy. The potential energy curve was calculated pointwise, with each point corrected for basis set superposition error using the full counterpoise correction.[10] Using Helgaker and co-workers two point extrapolation procedure,[11,12] the potential energy curve at the complete basis set limit was determined. The three calculated potential energy curves were entered as input into LeRoy's LEVEL program. [13] The obtained lowest few vibrational were least-squares fitted to the standard Morse equations to yield the spectroscopic constants reported in Table 3.6. As can be seen the extrapolated value of D_0'' is 164 cm $^{-1}$. Tests correlating the inner-valence orbitals of Au were conducted employing an d-awCVQZ-PP basis set[14] on Au. These tests indicated that the value of 164 cm^{-1} would be lowered by 5 cm^{-1} by core-valence correlation giving a "best" value of 160±5 cm^{-1} for D_0'' after comparison of the change in D_e'' between *d*-aVQZ and *d*-aCVQZ.

Table 3.6. Au-Ar $X^2\Sigma_{1/2}^+$ state calculated spectroscopic constants at RCCSD(T) level using specified basis set.

Basis Set	R_e/ Å	D_e''/ cm^{-1}	D_0''/ cm^{-1}	ω_e/ cm^{-1}	$\omega_e x_e$/ cm^{-1}	B_0/ cm^{-1}
d-aVQZ	3.790	161.9	149.9	24.6	0.96	0.034
d-aV5Z	3.770	168.8	156.5	25.1	0.96	0.035
d-aV∞Z[a]	3.730	176.5	163.9	25.8	0.97	0.036
d-aCV∞Z		171[a]	160[b]			

[a] Obtained using a two-point extrapolation procedure of Helgaker and co-workers – see text.

[b] Estimated values based on comparison of *d*-aCVQZ and *d*-aVQZ results.

3.4.2 Calculations on the excited states

In order to determine potentials for the $D^2\Pi_{1/2}$, $D^2\Pi_{3/2}$, and $E^2\Sigma_{1/2}^+$ excited states, a number of preliminary calculations had to be performed to assess possible effects the states arising from the $Au(^2D)$ + $Ar(^1S)$ asymptote may have on the higher energy states arising from the $Au(^2P)$ + $Ar(^1S)$ asymptote. If these potentials were shown not to cross the $D^2\Pi_{1/2}$, $D^2\Pi_{3/2}$, and $E^2\Sigma_{1/2}^+$ excited states near their potential energy minimum, the states arising from the $Au(^2D)$ + $Ar(^1S)$ asymptote could be justifiably neglected; thus saving time when performing complicated multireference calculations that also allow spin-orbit coupling to occur.

During preliminary calculations, the single reference RCCSD(T) method employing a aug-cc-pVDZ basis was used. The interaction between $Au(^2D_{5/2})$ + $Ar(^1S)$ yields $^2\Delta$, $^2\Pi$ and $^2\Sigma^+$ states, which then give rise to the $^2\Delta_{5/2}$, $^2\Delta_{3/2}$, $^2\Pi_{3/2}$, $^2\Pi_{1/2}$ and $^2\Sigma_{1/2}^+$ states when spin-orbit interaction is considered. The electronic configuration of the $Au(^2D)$ state is $(...5d^96s^2)$ in which the $5d$ orbitals are considerably smaller than the $6s$ ones. It is expected that the larger $6s$ orbitals dominates the weak interaction between the $Au(^2D)$ state and Ar, hence it is expected that the $^2\Delta$, $^2\Pi$ and $^2\Sigma^+$ "d hole" states will behave similar to one another. For ease it was felt that the $^2\Sigma^+$ state could be excluded from calculations leaving the following potential energy curves, where the parentheses give the Au configuration, to be determined: $^2\Sigma^+(...5d^{10}6s^1)$; $^2\Pi$, $^2\Delta$ $(...5d^96s^2)$; and $^2\Pi$ $(...5d^{10}6p^1)$. The results of these calculations are shown in Figure 3.6.
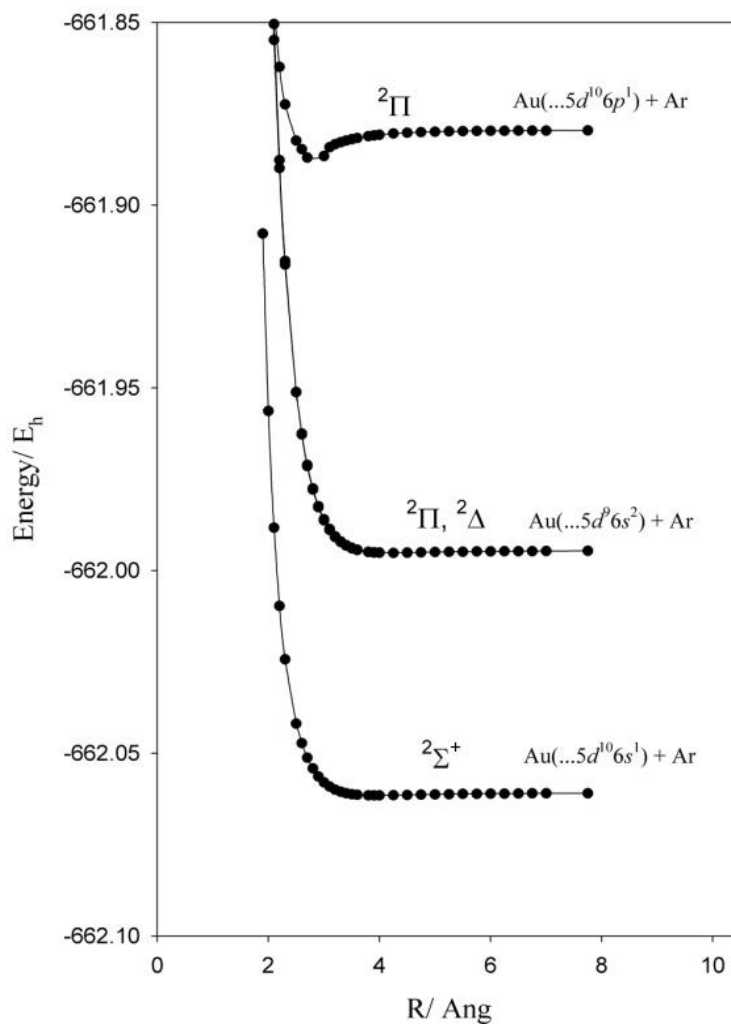
Figure 3.6. **RCCSD(T)/aug-cc-pVDZ calculated curves for Au-Ar electronic states arising from the lowest three atomic asymptotes. Note that the $A^2\Delta$ state lies slightly lower in energy than the $B^2\Pi$ state (but this is indiscernible on this scale), and that the $C^2\Sigma^+$ state was omitted from the calculations, but is expected to lie slightly above the $B^2\Pi$ state. The $E^2\Sigma^+$ state was also omitted, but lies above the $D^2\Pi$ state.**

From Figure 3.6 it can be clearly observed that the $^2\Delta$ and $^2\Pi$ states arising from the Au(^2D) + Ar(^1S) asymptote do not cross the higher lying $^2\Pi$ state close to it minimum but considerably further up the repulsive wall of its potential. It can therefore be concluded that effects from this crossing will be minimal leading to only minor perturbation in the energy of the observed states at least in the

-61-

Franck-Condon region. The $E^2\Sigma_{1/2}^+$ state, also originating from the Au(^2P) + Ar(^1S) asymptote, which has not been calculated, lies higher in energy than the $^2\Pi$ states (see later) and therefore is also not expected to be crossed close to its minimum. It can be seen that the two states arising from the Au(^2D) + Ar(^1S) asymptote are very close in energy, and almost parallel, it is therefore expected that the omitted $^2\Sigma^+$ state would follow these two states closely. Confirmation that a single-reference method is sufficient for the states considered comes from the large energy separation between them, observed in Figure 3.6; further evidence is that the T_1 diagnostic, a method for determining the quality of single-reference correlation methods,[15] is <0.03 in all cases.

From the results of the calculations it was observed that the states arising from the Au(^2D) + Ar(^1S) cross the $^2\Pi_\Omega$ (Ω = $^1/_2$, $^3/_2$) state potentials too far from the minimum to play a major part in the spectroscopy involved and therefore could be discounted in this set of calculations. For the CASSCF + MRCI calculations, the $5d$ and lower orbitals were constrained to be doubly occupied, allowing only the $6s$ or $6p$ electron to be active in the calculations for the respective states. However, the doubly occupied oribtals were allowed to relax during the CASSCF procedure. Although, this was expected to limit the amount of dynamic correlation included this was satisfactory as only a qualitative picture was required. The d-aVQZ basis sets described for the RCCSD(T) calculations were employed. The CASSCF + MRCI + Q energies of the two $^2\Sigma^+$ states and the $^2\Pi$ state, arising from the ...$6s^1$

and ...$6p^1$ configurations, were taken and used as the unperturbed energies in the spin-orbit calculations. These were then used for state-averaged CASSCF calculations to determine the spin orbit coupling at each R. The results of the calculations for the $D^2\Pi_{1/2}$, $D^2\Pi_{3/2}$ and $E^2\Sigma_{1/2^+}$ states are shown in Figure 3.7 and are discussed in conjunction with experimental results in Section 3.5.2.
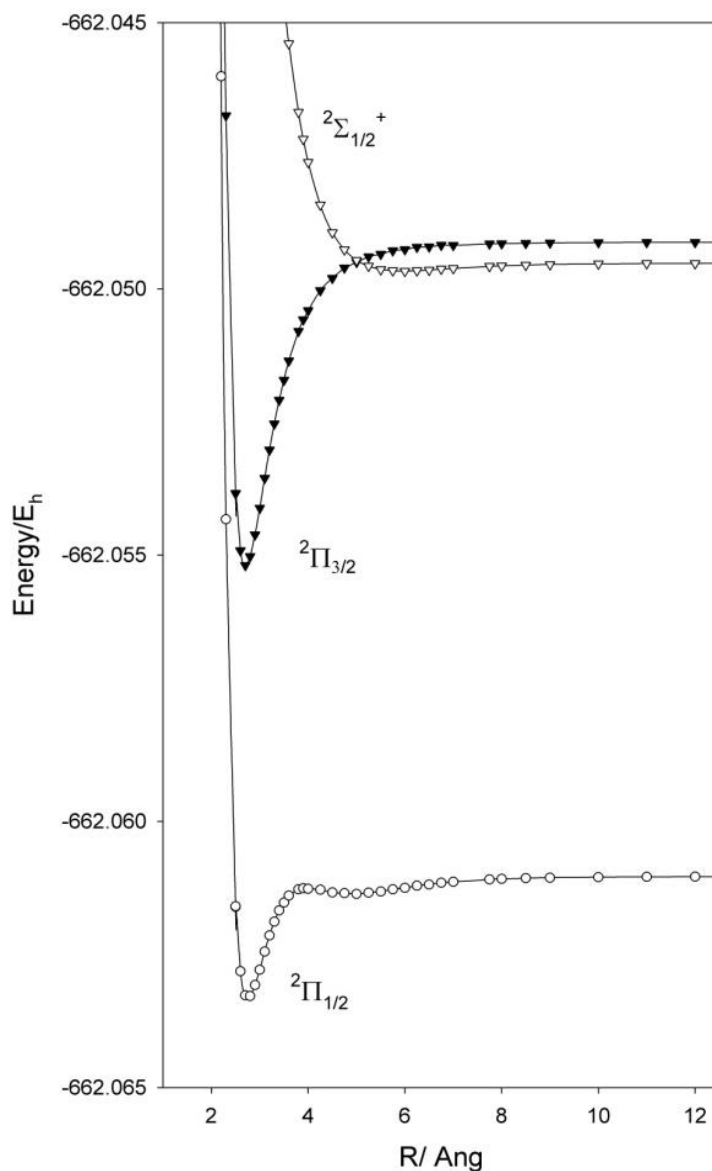
Figure 3.7. CASSCF + MRCI + Q calculations for Au-Ar employing the *d*-aVQZ basis set.

3.4.3 Accuracy of calculations

Before progressing any further it is at this point worthwhile informing the reader of the applicability of the level of theory that has been employed in the Au-Ar calculations and in subsequent Chapters for the other Au-RG complexes. Although a detailed assessment of the accuracy at a given level of theory is widely accepted as being difficult to establish (especially for molecular complexes and excited states),[16] owing to a heavy dependence on both the quality of the basis set and the type of interactions being calculated, RCCSD(T) is at the time of writing known as "the gold standard of computational methods." In strongly bound systems, given a sufficiently large basis set, the RCCSD(T) method is able to obtain an accuracy of ~4 kJ mol^{-1} for dissociation energies.[16] In the present Au-RG molecular complexes, however, the interactions considered are considerably weaker and therefore the associated error would be expected to be considerably greater. In these single reference method calculations the basis sets used are large and have been selected specifically for each of the interacting species. As mentioned above, calculations using Dunning style basis sets of quadruple and quintuple standard were performed that allowed the use of the two point extrapolation procedure of Helgaker and co-workers[11,12] to extrapolate to the basis set limit. Basis set superposition error was taken into account by employing the full counterpoise correction[10] pointwise.

The use of the multi-reference methods were used mainly to obtain a qualitative picture and therefore smaller basis sets were used in

comparison to calculations used where more quantitative values were required. The relative accuracy of multi-reference methods is as with the single reference methods, difficult to give explicitly as in addition to depending on the size of the basis set, these methods also depend on the size of the active space employed.[16]

3.4.4 Franck – Condon simulations of the $D^2\Pi_{3/2} \leftarrow X^2\Sigma_{1/2}^+$ Spectrum

The $D^2\Pi_{3/2}$ state appears relatively unaffected by the effects of the states arising from the $Au(^2D) + Ar(^1S)$ asymptote and any spin-orbit interactions, therefore an accurate determination of the $D^2\Pi$ state potential should yield accurate spectroscopic constants for the $D^2\Pi_{3/2}$ state which can then be reliably compared to experiment. With this in mind the $D^2\Pi$ potential energy curve was recalculated at the RCCSD(T)/d-aVQZ level, performing full counterpoise correction at each internuclear separation. Analysis of that curve yielded R_e = 2.621 Å, ω_e' = 116.4 cm^{-1}, $\omega_e'x_e'$ = 2.070 cm^{-1}, D_e' = 1781.8 cm^{-1}, and D_0' = 1724.1 cm^{-1}. Single point calculations at this R_e value, employing the d-aug-pV5Z basis set yielded a D_e' value of 1869.1 cm^{-1}, which can be extrapolated to yield D_e' = 1960.8 cm^{-1}; the latter gives D_0' = 1903 cm^{-1}. These calculated spectroscopic constants were used with those for the $X^2\Sigma_{1/2}^+$ state shown in Table 3.6 to produce the simulated spectrum shown in Figure 3.8, in which the intensity of the peaks in the simulated spectrum have been scaled in order to match the first couple of peaks in the experimental spectrum. As can been seen, vibrational hot bands corresponding to excitation from v'' = 1 and v'' = 2 have also been simulated which allows a rough vibrational

temperature of 15 K to be extracted using the Boltzmann distribution. In addition, by matching the vibrational spacing obtained in the simulation to those seen in the experimental spectrum an estimate of the absolute vibrational numbering can be obtained. This numbering has been used in Figure 3.8. It is interesting to note that the experimental peaks to higher energy are much more intense than those in the simulated spectrum, reasons for this will be discussed in Chapter 6.
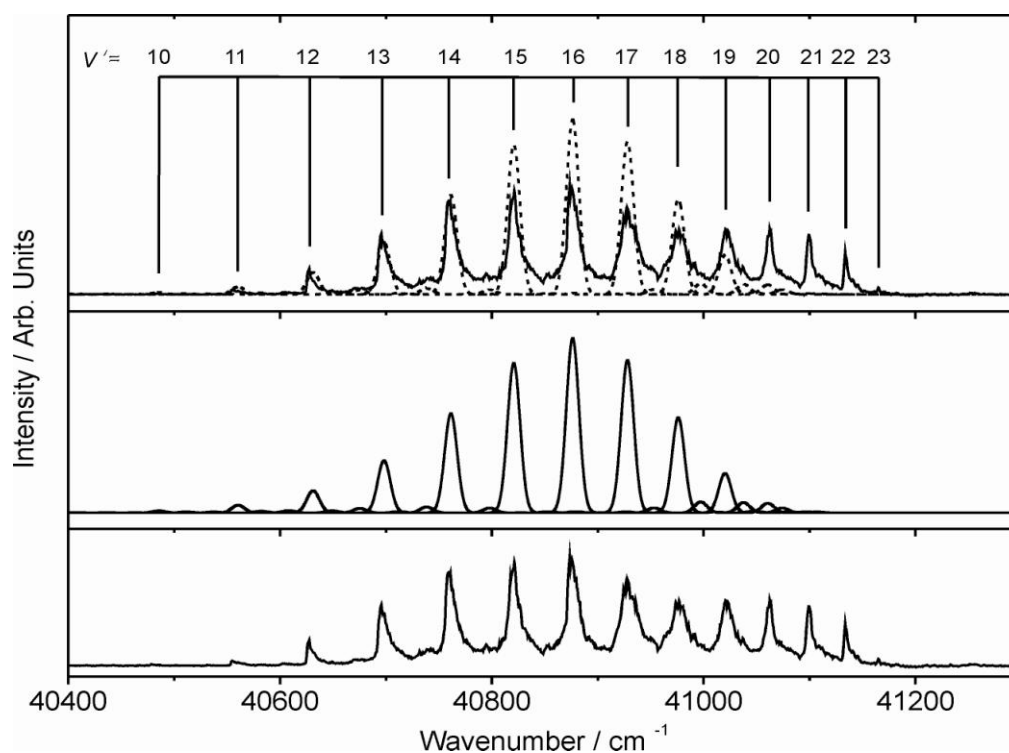
Figure 3.8. Franck-Condon simulation of the $D^2\Pi_{3/2} \leftarrow X^2\Sigma_{1/2}^+$ transition for Au–Ar, using calculated spectroscopic parameters for the $D^2\Pi$ state (see text) and calculated spectroscopic parameters for the $X^2\Sigma_{1/2}^+$ state given in Table 3.6. Bottom trace: experimental spectrum. Middle trace: simulation. Top trace: overlay of the experimental and simulated spectra.

3.5 Discussion

3.5.1 Au-Ar $X^2\Sigma_{1/2}^+$ state

The best calculated $X^2\Sigma_{1/2}^+$ ground state dissociation energy is 160±5 cm^{-1} which is in reasonable agreement with values determined using D_L from a LeRoy-Bernstein extrapolation of the experimentally observed vibrational levels in the $D^2\Pi_{1/2}$ state, in conjunction with the Au ($^2P_{1/2} \leftarrow {}^2S_{1/2}$) atomic transition. This value is also in concurrence with the lower bound estimate of 130 cm^{-1} quoted by Knight *et al.* It is suspected that the value of 211cm^{-1} determined *via* spectroscopic constants determined from analysis of the $D^2\Pi_{3/2}$ overestimates D_0''. A more recent value for D_0'' of 149 ± 13 cm^{-1} obtained *via* velocity map imaging experiments on the Au-RG complexes[17] is also in excellent agreement with the theoretical value. The identification of hot bands arising from $v''=1$ and $v''=2$ levels in Figure 3.1 and Figure 3.2, confirmed by studies probing different regions within the molecular beam, allows an experimental value for the 1-0 and 2-1 vibrational spacings in the ground state to be derived. These experimental values of 24±2 cm^{-1} for the 1-0 spacing and 22 ±2 cm^{-1} for the 2-1 spacing are in excellent agreement with the corresponding theoretical values of 23.9 and 21.9 cm^{-1} respectively confirming the assignment of these vibrational features.

3.5.2 Au-Ar $D^2\Pi_{1/2}$ state

The $D^2\Pi_{1/2} \leftarrow X^2\Sigma_{1/2}^+$ spectrum exhibits an obvious discontinuity in the vibrational spacings observed, in addition to a distinct change in

the rotational profile of the peaks. The observation that the rotational profile changed going through the spectrum was confirmed by a number of band profile simulations, the results of which are shown in Table 3.7.

Table 3.7. Rotational constants required to obtain a theoretical peak shape and width similar to that observed experimentally for the $D^2\Pi_{1/2}$ state. B_0'' was determined theoretically as 0.036 cm^{-1}. The dashed line indicates the change in regime within the progression.

PEAK	Position (cm^{-1})	B' (cm^{-1})
N	37137.7	peak too small
$n+1$	37200.1	0.068
$n+2$	37258.4	0.075
$n+3$	37309.8	0.080
$n+4$	37354.3	0.088
$n+5$	37389.6	0.090
$n+6$	37416.3	0.058
$n+7$	37436.2	0.038
$n+8$	37450.4	0.039
$n+9$	37462.6	0.040
$n+10$	37473.2	0.042
$n+11$	37483.5	peak too small

It was found that the broader peaks to the lower energy end of the spectrum required rotational constants significantly larger than that of the ground state to give the required line width and shapes, conversely the higher energy features required a rotational constant similar to that of the ground state. For these simulations the resolution of the laser and temperature were kept constant at 0.6 cm^{-1} and 6 K respectively; while it should be noted that the actual resolution is expected to be better than 0.6 cm^{-1} the effects of power broadening is likely to have increased the observed line widths.

A plausible explanation for the observed peculiarities of this spectrum is that the reported vibrational levels originate from two regions of the surface with significantly different internuclear separations. This interpretation fits well with information obtained from analysis of the experimental results, in which the LeRoy-Bernstein method achieves values of D_L considerably closer to that expected from theory using the calculated ground state dissociation value and Au ($^2P_{1/2} \leftarrow\, ^2S_{1/2}$) atomic transition, by analysing different sections of the progression separately. A number of possibilities for the formation of these two regions were initially hypothesised. One possible mechanism is that these two regions occur *via* an avoided curve crossing. The calculations looking at a potential curve crossing of the $D^2\Pi$ states from lower lying states, shown in Figure 3.6, indicate that any potential crossing would be high on its repulsive limb and are therefore unlikely to cause the effect observed in the spectrum. There is also the possibility of a strongly bound higher lying state cutting through the $D^2\Pi_{1/2}$ state potential and there is indeed the ^4P state arising from a [Xe]$4f^{14}5d^96s^16p^1$ configuration at 42163.5 cm^{-1} that could potentially lead to states that could cross the $D^2\Pi_{1/2}$ state. However, this can be disregarded as any states in this region will include some degree of s character, suggesting they are unlikely to be bound by the ~5000 cm^{-1} required to cross the $D^2\Pi_{1/2}$ state potential.

Another hypothesized mechanism for the formation of these two regions is through the penetration of the rare gas atom through the outermost atomic orbital; such a mechanism has been previously

observed for Hg-Ar[18] and NO-RG.[19] The formation of the two regions in this case is through an initial long range interaction resulting in a shallow minimum at large R, followed by an increase in energy as the RG approaches and penetrates the outer electron orbital. On penetration of the outer electron orbital the RG subsequently interacts with the cationic core of either the Hg or NO. This mechanism seems unlikely as in the two cases highlighted the electron is located in a large orbital; hence Rydberg in character, whilst in the present case the electron is located in a valence orbital. Additionally, the two extrapolation procedures performed on the two regions of the $D^2\Pi_{1/2}$ progression, indicate that the dissociation energies of the two sets of vibrational levels are in close proximity; this would be unlikely to happen if one of the progressions was cationic in nature.

It is at this point the results of the calculations in which spin-orbit interactions are allowed to occur are considered. From Figure 3.7 it is clear that mixing, owing to spin-orbit interactions, between the $D^2\Pi_{1/2}$ and the $E^2\Sigma_{1/2}^+$ state has a considerable effect on both of the potential energy curves of these states. In the absence of this spin-orbit interaction it would be expected that the potential energy curves of the $D^2\Pi_{1/2}$ and $D^2\Pi_{3/2}$ states would be identical, but as is observed there are obvious differences between them. The calculations indicate that the $D^2\Pi_{1/2}$ is considerably less bound than the $D^2\Pi_{3/2}$ state (447 cm^{-1} and 1332 cm^{-1} respectively) owing to the spin-orbit mixing with the repulsive limb of the $E^2\Sigma_{1/2}^+$ state. Additionally, the attractive limb of the $D^2\Pi_{1/2}$ potential can be seen to be perturbed, resulting in a

shallow minimum bound by ~23.5 cm^{-1}. The effects on the $E^2\Sigma_{1/2}{}^+$ state potential curve are not as apparent, owing to the minimum of the $D^2\Pi_{1/2}$ state being at a separation corresponding to high on the repulsive region of the $E^2\Sigma_{1/2}{}^+$ potential. The difference in energy between the $E^2\Sigma_{1/2}{}^+$ and $D^2\Pi_{3/2}$ state potentials at large R can be attributed to the $6p\sigma$ electron density being located along the internuclear axis therefore increasing the attraction to Ar through dispersive interactions at long R; however, as R decreases, electron-electron repulsion quickly increases resulting in this state being bound by only 32 cm^{-1}. In contrast to this, the $6p\pi$ electron density is located off the internuclear axis allowing the Ar atom to penetrate to much shorter R before repulsion sets in. This results in a considerably stronger interaction as the Ar atom can interact with the Au$^+$ core. The two potentials are expected eventually to converge at a longer separation, though there may be a small energy offset observed for the two calculated potentials at the level of theory employed. A D_e value for the $X^2\Sigma^+{}_{1/2}$ state at this level of theory was determined to be ~147 cm^{-1}, which is in reasonable agreement with RCCSD(T)/d-aug-cc-pVQZ result of ~162 cm^{-1} discussed above suggesting that much of the dynamic electron correlation energy is being recovered in the RCCSD(T) procedure, as expected.

The results of the spin-orbit calculations give an explanation of the occurrence of two regions in the $D^2\Pi_{1/2}$ state potential. However, a closer examination of the observed spectrum brings in to question the presence of a double minimum suggested by the calculations. If a

double minimum was present a number of overlapping vibrational features might be expected to be observed, which they are not. In the spin-orbit calculations the $^2P_{3/2}$ – $^2P_{1/2}$ separation ~2600 cm^{-1} differs considerably to the experimental value of 3815.4 cm^{-1}.[20] Examination of the calculated Au($^2P_{3/2}$) – Ar($^2S_{1/2}$) and Au($^2P_{1/2}$) – Ar($^2S_{1/2}$) separations, ~41040 and 38470 cm^{-1} respectively to the experimental separations[20] 41174 and 37358.9 cm^{-1} suggest that it is the calculated $D^2\Pi_{1/2}$ state that is the responsible for the observed discrepancy. These observations suggest that the states arising from the Au(^2D) + Ar(^1S) asymptote (and possibly others) will have a measurable effect on the $D^2\Pi_{1/2}$ state while the $D^2\Pi_{3/2}$ state will be relatively unaffected. Although it is not expected that the inclusion of these interactions would have a major effect on the overall potential it could be argued that the inclusion of these interactions would result in the $D^2\Pi_{1/2}$ potential, currently calculated to exhibit a shallow minimum, to become more shelf like. This shelf like potential would still explain the observed discontinuity in the vibrational spacing and the change in the rotational profile of features but in addition would also account for the lack of observed overlapping of the vibrational features. Schematic potentials curves depicting the evolution of the shelf state in the $D^2\Pi_{1/2}$ caused by mixing with the $E^2\Sigma_{1/2}^+$ are shown in Figure 3.9.
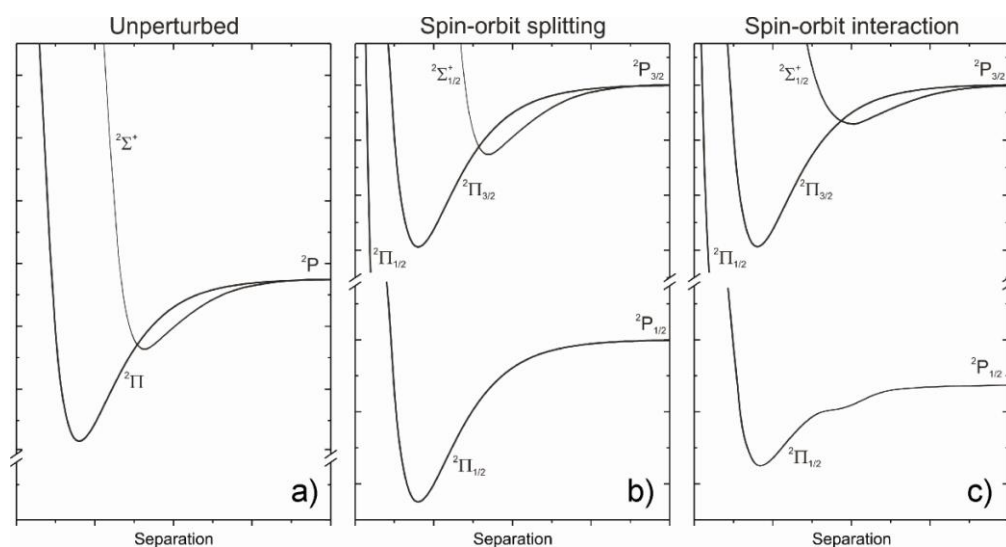
Figure 3.9. Schematic potential energy curves depicting the evolution of the shelf state. a) The pure Π and Σ curves b) The effects of spin-orbit splitting is shown c) Inclusion of spin-orbit interactions showing the mixing between states of the same Ω value.

3.5.3 Au-Ar $D^2\Pi_{3/2}$ state

The spectrum obtained for the $D^2\Pi_{3/2}$ state was more regular in appearance than that obtained for the $D^2\Pi_{1/2}$, as it is not affected by the spin-orbit mixing responsible for the perturbation of the $D^2\Pi_{1/2}$ potential. The values obtained from experimental data through a Birge-Sponer analysis for ω_e' and $\omega_e'x_e'$ are in line with both those obtained through analysis of the calculated pure $^2\Pi$ curve, expected to represent the $D^2\Pi_{3/2}$ potential accurately, and those reported by Knight *et al.*[1] However, the Birge-Sponer analysis considerably underestimates D_0' value in comparison to that obtained theoretically; this underestimation is carried through to an underestimation of D_0''. This underestimation can be attributed to the failure of the Morse approximation at higher vibrational levels as long range interactions become important.

Attempts were again made to simulate the rotational profiles of the peaks. As can be seen in Table 3.8 the simulated bands were always narrower than the experimental bands, even with an unreasonable linewidth of 0.8 cm^{-1}. This is expected to be a result of power broadening or predissociation owing to J-dependent coupling of the $\Omega=^3/_2$ v' levels into the $\Omega=^1/_2$ continuum states; a power-dependence study was performed but was not conclusive, owing to poor signal to noise on reduction of the power.

Table 3.8. Rotational constants required to obtain a theoretical peak shape and width similar to that observed experimentally for the $D^2\Pi_{3/2}$ state. B_0'' was determined theoretically as 0.036 cm^{-1}.

PEAK	Position (cm^{-1})	B' (cm^{-1})
$n+2$	40557.2	0.065
$n+3$	40628.4	0.068
$n+4$	40696.6	0.080
$n+5$	40760.7	0.085
$n+6$	40819.9	0.085
$n+7$	40876.0	0.090
$n+8$	40928.1	0.093
$n+9$	40978.2	0.100
$n+10$	41021.2	0.085
$n+11$	41061.3	0.062
$n+12$	41099.3	0.060
$n+13$	41133.3	0.050

3.5.4 Au-Ar $E^2\Sigma_{1/2}^+$ state

The $E^2\Sigma_{1/2}^+$ state, like the $D^2\Pi_{3/2}$ state, originates from the Au($^2P_{3/2}$) + Ar($^1S_0$) asymptote. The potential minimum of the $E^2\Sigma_{1/2}^+$ state is expected to be considerably shallower and to longer R in respect to the

$D^2\Pi_{3/2}$ state minimum. Scans were carried out close to and to higher energy than the atomic transition but no evidence of any features in this region were seen, consistent with the observations of Knight *et al.* Though the potential is expected to be quite weakly bound, owing to the perturbation observed in the $D^2\Pi_{1/2}$ potential, some vibrational levels might still be expected to be supported. It therefore seems likely that the failure to observe this state could be the result of the bound levels being outside the Franck-Condon window or that the vibrational levels are completely dissociative on the timescale of our experiment. One possible mechanism in which dissociation could occur is through coupling into the $D^2\Pi_{1/2}$ state continuum.

3.6 Conclusions

Spectra have been recorded in the energetic region corresponding to the Au atomic transitions $^2P_J \leftarrow {}^2S$. The two spectra recorded were similar to those previously recorded by Knight *et al.* However, the spectra within this work demonstrates an additional feature to higher energy for the $D^2\Pi_{1/2} \leftarrow X^2\Sigma^+_{1/2}$ spectrum, whilst the $D^2\Pi_{3/2} \leftarrow X^2\Sigma^+_{1/2}$ spectrum has a superior signal to noise ratio particularly noticeable at the higher energy end of the spectrum. The discontinuity observed in the $D^2\Pi_{1/2} \leftarrow E^2\Sigma^+_{1/2}$ spectrum has been attributed to a perturbation in the $D^2\Pi_{1/2}$ state potential. Calculations suggested that this perturbation was in the form of a double minimum, however, more detailed calculations are expected to give rise to a potential containing a shelf-like region on its attractive limb that would be more consistent with experimental observations. The perturbation has been concluded

to arise through a strong spin-orbit interaction of the $D^2\Pi_{1/2}$ state with the $E^2\Sigma_{1/2^+}$ state.

As expected, the $D^2\Pi_{3/2}$ state was observed to be unaffected by this spin-orbit interaction, with the shape of the potential found to be accurately described by the calculated pure $^2\Pi$ potential. Rotational simulations suggest that the vibrational features are in the $D^2\Pi_{1/2} \leftarrow X^2\Sigma^+_{1/2}$ spectrum are broader than would be expected, indicative of power broadening or possible predissociation of the vibrational levels into the $D^2\Pi_{1/2}$ continuum. An assignment for the absolute vibrational numbering is also given; determined by the matching of experimental and simulated vibrational spacings.

Despite scans in the appropriate energetic region the $E^2\Sigma_{1/2^+} \leftarrow X^2\Sigma^+_{1/2}$ transition was not observed, in accordance with observations of Knight *et al.*,[1] although the potential is expected to contain only a shallow well it is still expected to contain a number of vibrational levels. The failure to observe this state may be attributed to dissociation into the $D^2\Pi_{1/2}$ continuum although the possibility of the minimum being located outside the Franck-Condon region has not been ruled out.

Calculations on the ground state have yielded a D_0'' value of 160±5 cm^{-1} which is in excellent agreement with experimentally-derived values. The identification of vibrational hot bands has allowed the 1-0 and 2-1 vibrational spacings in the $X^2\Sigma^+_{1/2}$ state to be experimentally

derived; these values are in excellent agreement with those obtained through theory.

References

[1] A. M. Knight, A. Stangassinger and M. A. Duncan, *Chem. Phys. Lett.* 1997, **273**, 265.

[2] http://physics.nist.gov/cgi-bin/Compositions/stand_alone.pl

[3] A. M. Ellis, M. Feher, and T. G. Wright, *Electronic and Photoelectron Spectroscopy Fundamentals and Case Studies,* Cambridge University Press, Cambridge, 2005.

[4] P. F. Bernath, *Spectra of Atoms and Molecules*, Oxford University Press, Oxford, 1995.

[5] P. W. Atkins, *Physical Chemistry Third Edition,* Oxford University Press, Oxford, 1986.

[6] R. J. LeRoy and R. B. Bernstein, *J. Chem. Phys.,* 1970, **52** (8), 3869.

[7] R. J. LeRoy and R. B. Bernstein, *J. Mol. Spect.,* 1971, **37**, 109.

[8] MOLPRO is a package of *ab initio* programs written by H. J. Werner, P. J. Knowles and others.

[9] K. A. Peterson and C. Puzzarini, *Theor. Chim. Acta.*, 2005, **114**, 283.

[10] S. F. Boys, F. Bernardi, *Mol. Phys.,* 1970, **19**, 553.

[11] T. Helgaker, W. Klopper, H. Koch and J. Noga, *J. Chem. Phys.*, 1997, **106**, 9639.

[12] A. Halkier, T. Helgaker, P. Jÿrgensen, W. Klopper, H. Koch, J. Olsen and A. K. Wilson, *Chem. Phy. Lett.*, 1998, **286**, 243.

[13] R. J. LeRoy, LEVEL 7.2 - *A computer program for solving the radial Schrödinger equation for bound and quasibound levels, and calculating various expectation values and matrix elements.* (University of Waterloo Chemical Physics Research Program Report CP-555R (2000)).

[14] This basis set was not available directly in the MOLPRO library, and so it was constructed by Dr. E. Lee manually adding the additional tight functions from the available cc-pCVQZ basis set, to the available aug-cc-pVQZ one.

[15] T. J. Lee and P. R. Taylor, *Int. J. Quant.Chem.*, 1989, **23**, 199.

[16] F. Jensen, Introduction to computational chemistry Second Edition, John Wiley & Sons Ltd., Chichester, 2007.

[17] W. S. Hopkins, A. P. Woodham, S. R. Mackenzie, R. J. Plowright and T. G. Wright, *J. Chem. Phys.*, submitted.

[18] M. -C. Duval, O. B. D'Azy, W. H. Breckenridge, C. Jouvet and B. Soep, *J. Chem. Phys.,* 1986, **85**(11), 6324.

[19] D. E. Bergeron, A. Musgrave, R. T. Gammon, V. L. Ayles, J. A. E. Silber and T. G. Wright, *J. Chem. Phys.,* 2006, **124**, 214302.

[20] http://physics.nist.gov/PhysRefData/Handbook/Tables/goldtable5.htm